



Line Formation of Raman-scattered He II λ 4851 in an Expanding Spherical H I Shell in Young Planetary Nebulae

Bo-Eun Choi¹, Seok-Jun Chang^{1,2}, Ho-Gyu Lee², and Hee-Won Lee¹ ¹ Department of Physics and Astronomy, Sejong University, Republic of Korea; hwlee@sejong.ac.kr² Korea Astronomy and Space Science Institute, Republic of Korea

Received 2019 November 23; revised 2019 December 10; accepted 2019 December 10; published 2020 January 20

Abstract

We investigate line formation of Raman-scattered He II at 4851 Å in an expanding neutral, spherical shell that surrounds a point-like He II source located at the center. A new grid-based Monte Carlo code is used to take into consideration the H I density variation along each photon path. In the case of a monochromatic He II emission source, the resultant line profiles are characterized by an asymmetric double-peak structure with a tertiary peak and a significant red tail that may extend to the line centers of He II λ 4859 and H β . The peak separation corresponds to the expansion velocity, which we consider is in the range 20–40 km s^{−1} in this work. Tertiary red peaks are formed as a result of multiple Rayleigh reflections at the inner surface of a hollow, spherical shell of H I. Due to a sharp increase of scattering cross section near resonance, the overall Raman conversion efficiency is significantly enhanced as the expansion speed increases. In the case of a He II line source with a Gaussian line profile with an FWHM of 30–70 km s^{−1}, we obtain distorted redward profiles that are due to the increasing redward cross section of H I. A simple application to the young planetary nebula IC 5117 is consistent with a neutral shell expanding with a speed \sim 30 km s^{−1}.

Unified Astronomy Thesaurus concepts: Planetary nebulae (1249); Radiative transfer (1335); Stellar mass loss (1613)

1. Introduction

Stars with mass less than 8 M_{\odot} lose a significant fraction of their mass via heavy stellar winds in the asymptotic giant branch (AGB) phase, before they enter the planetary nebula (PN) stage (Höfner & Olofsson 2018). A PN consists of a hot central star and an expanding shell that is photoionized by strong far-UV radiation originating from the hot central star. High-spatial-resolution imaging surveys of PNe reveal that a variety of nebular morphologies appear, including spherical, elliptical, bipolar, and point-symmetrical shells (Sahai et al. 2011; Hsia et al. 2014). According to the generalized interaction wind model, the various shell structures may result from the interaction of a fast wind from the hot central star and a slow wind formed in the AGB phase (Kwok et al. 1978). Depending on the column density along a line of sight from the central star of a PN, the surrounding nebula can be either ionization bounded or matter bounded. In the former case, the distribution and the kinematics of H I in the circumnebular region are very important for understanding the mass-loss process in the AGB stage and the evolution of PNe.

There have been a number of attempts to detect H I in PNe using the 21 cm hyperfine structure line. It is a very difficult task to measure the H I mass in a PN using the 21 cm line because of confusion arising from the galactic emission. The first successful detection of atomic hydrogen in PNe was made in NGC 6302 by Rodríguez et al. (1985), who measured the H I mass \sim 0.06 M_{\odot} . Rodríguez et al. (2002) also reported the detection of H I emission from the Helix Nebula (NGC 7293), noting that the radial velocity of H I ranges by \sim 50 km s^{−1}.

Another powerful tool to probe H I components is Raman-scattered features formed through Raman scattering of far-UV photons with hydrogen atoms. Nonrelativistic interaction of a far-UV photon and an atomic electron can be classified into Rayleigh and Raman scattering. In the former case, the initial

and final states of the electron are the same, so the wavelengths of the incident and outgoing photons are identical. In the case of Raman scattering, the final electronic state differs from the initial state, resulting in an outgoing photon with a wavelength different from that of the incident photon. In the vicinity of mass-losing stellar objects, Raman scattering is known to operate when far-UV radiation more energetic than Ly α is incident on a thick neutral region. Raman-scattered features therefore may provide extremely useful information on the distribution and kinematics of neutral material associated with the mass-loss processes occurring in the late stage of stellar evolution (Nussbaumer et al. 1989).

The first astrophysical identification of Raman scattering with atomic hydrogen was proposed in symbiotic stars, which are wide binary systems of a mass-losing giant and a hot star, usually a white dwarf (Kenyon 1986). About one-half of symbiotic stars show emission features at 6830 Å and at 7088 Å with width $\Delta v \sim$ 100 km s^{−1} (Allen 1980; Akras et al. 2019). Schmid (1989) proposed that they are formed as a result of Raman scattering of the far-UV doublet O VI $\lambda\lambda$ 1032 and 1038 with atomic hydrogen. Symbiotic stars are ideal objects for Raman scattering, because a thick neutral region is found near the mass-losing giant and copious O VI line photons are generated around the mass-accreting white dwarf.

Another interesting application of atomic Raman scattering is found in far-UV He II emission lines. Hydrogen-like ions share the same energy level structure with level spacing proportional to $Z^2(n_1^{-2} - n_2^{-2})$, where n_1 and n_2 are principal quantum numbers and Z is the atomic number. In particular, He II emission lines resulting from transitions to $n = 2$ levels from $n = 2k$ levels have wavelengths slightly shortward of the H I Lyman series associated with the kp state. Therefore, Raman-scattered He II features are formed blueward of H I Balmer lines. For example, far-UV He II emission lines at

1025 Å, 972 Å, and 949 Å are Raman scattered to form emission features at 6540 Å, 4851 Å, and 4332 Å, respectively.

The first detection of a Raman-scattered He II feature was reported by van Groningen (1993), who found a broad emission feature at 4851 Å in the symbiotic nova RR Telescopii. Subsequently, Raman-scattered He II features were found in the symbiotic stars V1016 Cygni, HM Sagittae, and V835 Centauri (Lee et al. 2001; Birriel 2004). Assuming the case B recombination theory is valid for He II lines, one can deduce the flux of He II λ 972 by measuring the flux of optical He II λ 4859 or He II λ 4686 and hence calculate the Raman conversion efficiency, defined as the photon number ratio of He II λ 972 and Raman-scattered He II λ 4851.

Young PNe also satisfy the requirement for operation of Raman scattering of He II with the presence of a strong He II emission region near the hot central white dwarf surrounded by a thick neutral region as a result of recent mass loss. Péquignot et al. (1997) reported their discovery of Raman-scattered He II in the young PN NGC 7027. Raman He II features were also found in a number of young PNe, including NGC 6302 (Groves et al. 2002), IC 5117 (Lee et al. 2006), and NGC 6790 (Kang et al. 2009). It is quite notable that molecular lines have been detected in all of these young PNe with Raman-scattered He II. For example, H₂ was observed in NGC 7027, NGC 6302, and IC 5117 (Kastner et al. 1996), and polycyclic aromatic hydrocarbon was detected in NGC 6790 (Smith & McLean 2008). The presence of molecular components in these objects indicates their recent entrance on the PN stage. In this regard, Raman-scattered He II features are great implements for studying the circumnebular HI region of young PNe.

Jung & Lee (2004) performed Monte Carlo simulations to investigate line formation of Raman-scattered He II in a static neutral medium illuminated by a He II emission source. Basic results obtained from studies of line formation in static media have been used to derive the content of neutral material surrounding the hot central stars of PNe. However, in young PNe, the neutral and molecular components are supposed to move radially outward with a speed that is comparable to the escape velocity $v_{\text{esc}} \sim 20 \text{ km s}^{-1}$ of a typical giant star. In this environment, the redward line-center shift will be enhanced, leading to significant distortion in the line profile. In this article, we use a grid-based Monte Carlo code to investigate line formation of Raman-scattered He II λ 4851 with a moving HI spherical shell.

This paper is organized as follows. Basic atomic physics, scattering geometry, and Monte Carlo procedures are described in Section 2. We present our results in Section 3, which is followed by a summary and discussion in the final section.

2. Atomic Physics and Radiative Transfer

2.1. Cross Section and Branching Ratios

Regarded as a two-body system, the reduced mass of He II is slightly heavier than that of HI by a factor $3m_e/(4m_p) \sim 4.08 \times 10^{-4}$, where m_e and m_p are the electron and proton masses, respectively. This slight excess in reduced mass leads to the energy level spacing of He II being larger than that of HI by a factor slightly in excess of 4 (Lee et al. 2001). More quantitatively, the line center of He II λ 972 is blueward of HI Ly γ by $\Delta V = -124 \text{ km s}^{-1}$.

The cross sections for Rayleigh and Raman scattering are given as an infinite sum of the probability amplitudes

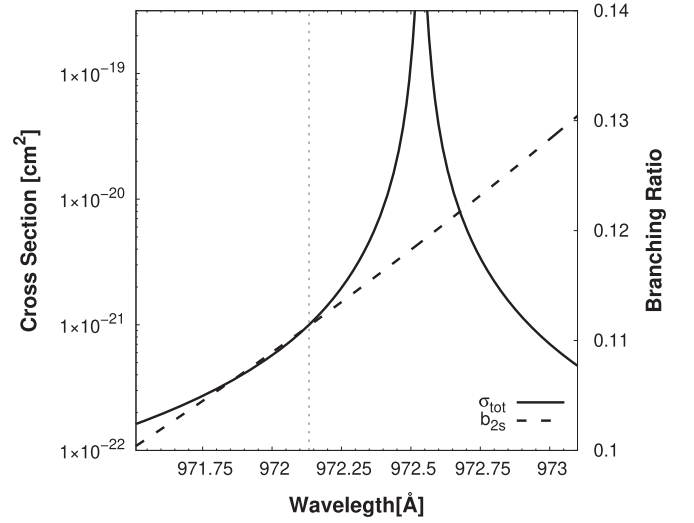


Figure 1. Cross section and branching ratio of far-UV radiation near He II λ 972. The solid curve shows the total cross section, and the dashed line shows the branching ratio of the transition to the $2s$ level. The dotted vertical line shows the rest wavelength of the He II λ 972 emission line.

associated with all bound and free p states, which is known as the Kramers–Heisenberg formula (e.g., Sakurai 1967; Bethe & Salpeter 1967):

$$\begin{aligned} \frac{d\sigma}{d\Omega} = & r_e^2 \left(\frac{\omega'}{\omega} \right) \left| \delta_{AB}(\epsilon^{(\alpha)} \cdot \epsilon^{(\alpha')}) \right. \\ & + \frac{1}{m_e} \sum_I \left(\frac{(\mathbf{p} \cdot \epsilon^{(\alpha')})_{BI} (\mathbf{p} \cdot \epsilon^{(\alpha)})_{IA}}{E_I - E_A - \hbar\omega} \right. \\ & \left. \left. + \frac{(\mathbf{p} \cdot \epsilon^{(\alpha)})_{BI} (\mathbf{p} \cdot \epsilon^{(\alpha')})_{IA}}{E_I - E_A + \hbar\omega'} \right) \right|^2. \end{aligned} \quad (1)$$

Here, $r_e = e^2/m_e c^2 = 2.82 \times 10^{-13} \text{ cm}$ is the classical electron radius. The initial and final electronic states are represented by A and B , and I stands for an intermediate state, which is one of p states in the case of electric dipole processes. In the case of Rayleigh scattering, $A = B = |1s\rangle$, and in the case of Raman scattering, B is one of $2s$, $3s$, and $3d$. The Kronecker delta symbol δ_{AB} vanishes in the case of Raman scattering, whereas it becomes unity in the case of Rayleigh scattering. The angular frequencies of the incident and outgoing photons are denoted by ω and ω' , respectively. The polarization vectors of the incident and outgoing photons are denoted by $\epsilon^{(\alpha)}$ and $\epsilon^{(\alpha')}$, respectively.

The term $(\mathbf{p} \cdot \epsilon^{(\alpha)})_{IA}$ is the matrix element of the momentum operator component along the polarization vector $\epsilon^{(\alpha)}$ between the states I and A , which is proportional to the dipole transition amplitude. The explicit values of the matrix element can be found in Karzas & Latter (1961). These matrix elements can also be computed using the Dalgarno–Lewis method, where the cross sections are expressed as a convolution of the final-state wavefunction and the Green’s functions associated with the Rayleigh and Raman interactions (e.g., Sadeghpour & Dalgarno 1992).

In Figure 1, we show the total cross section σ_{tot} , where the total cross section is the sum of cross sections of Rayleigh and Raman scattering. In the same figure, the branching ratio b_{2s} for Raman scattering into the $2s$ state is also shown by a dotted

line. In the wavelength range shown in the figure, the branching ratio into the $2s$ state ranges between 0.1 and 0.13. It is clearly notable that both the cross section and the branching ratio are rapidly increasing in the wavelength range shown in the figure.

For Raman-scattered He II $\lambda 4851$, the proximity to $1s-4p$ resonance of H I implies that the dominant contribution comes from the probability amplitude associated with the dipole expectation values corresponding to the $1s \rightarrow 4p \rightarrow 2s$ transition. If we approximate the total scattering cross section (sum of Rayleigh and Raman scattering cross sections) by a Lorentzian function neglecting p states other than $4p$, we obtain

$$\sigma_{\text{Ram}}(\lambda) \simeq \sigma_0 \left(\frac{\lambda_0}{\lambda - \lambda_0} \right)^2, \quad (2)$$

where $\sigma_0 = 0.17 \times 10^{-27} \text{cm}^2$ (Jung & Lee 2004). At the line center of He II $\lambda 972$, it turns out that the total scattering cross section is

$$\sigma_{\text{tot,He II } 972} = 9.1 \times 10^{-22} \text{cm}^2, \quad (3)$$

with the branching ratio into the final $2s$ state being 0.11. Therefore, we may roughly expect that Raman scattering may result once out of nine Rayleigh scattering events.

From energy conservation, the wavelength λ_f of a Raman-scattered photon is related to the λ_i of the incident far-UV photon by

$$\frac{1}{\lambda_f} = \frac{1}{\lambda_i} - \frac{1}{\lambda_{\text{Ly}\alpha}}, \quad (4)$$

where $\lambda_{\text{Ly}\alpha}$ is the line center wavelength of H I Ly α . In the case of He II $\lambda 972$, the line center wavelength averaged over all fine structures is $\lambda_{i,\text{He II } 972} = 972.134 \text{\AA}$ (Lee et al. 2006), resulting in the atomic line center of Raman-scattered He II $\lambda 4851$ at

$$\lambda_{c,4851} = 4851.29 \text{\AA} \quad (5)$$

with a consideration of the air index of refraction $n_{\text{air}} = 1.000279348$ and $\lambda_{\text{Ly}\alpha} = 1215.67 \text{\AA}$ (Jung & Lee 2004). From the line center of H β , the Doppler factor of the Raman-scattered He II $\lambda 4851$ is

$$\Delta V_{\text{Ram}4851} \simeq -619 \text{ km s}^{-1}. \quad (6)$$

One important spectroscopic property of Raman-scattered features lies with line broadening by a factor λ_o/λ_i , which is attributed to the inelasticity of scattering. Given that $\lambda_{\text{Ly}\alpha}$ is a constant, the line-broadening relation for Raman scattering is obtained by differentiating Equation (4), which leads to

$$\frac{\Delta \lambda_f}{\lambda_f} = \left(\frac{\lambda_f}{\lambda_i} \right) \frac{\Delta \lambda_i}{\lambda_i}. \quad (7)$$

For example, if a hydrogen atom moves away from a He II ion with a speed $\Delta v = +20 \text{ km s}^{-1}$, the wavelength shift $\Delta \lambda_f$ of a Raman-scattered He II $\lambda 4851$ is

$$\Delta \lambda_f = 1.62 \text{\AA}, \quad (8)$$

which would correspond to a new Doppler shift $\Delta v = +100 \text{ km s}^{-1}$ with respect to the Raman-scattered He II line center. If the relative speed is $\Delta v = +124 \text{ km s}^{-1}$ between H I and He II, then the He II $\lambda 972$ photon is regarded as a Ly γ photon in the rest frame of the hydrogen atom, and Raman scattering becomes effectively resonance scattering of Ly γ .

A far-UV He II $\lambda 972$ line photon incident on a thick neutral region may be Rayleigh scattered several times before it may escape from the region. Rayleigh scattering of a far-UV photon is described as elastic in the rest frame of the scatterer, so in the observer's rest frame the wavelength of a Rayleigh-scattered photon changes according to

$$\Delta \lambda = \lambda_i \left[\frac{(\hat{\mathbf{k}}_i - \hat{\mathbf{k}}_f) \cdot \mathbf{v}_{\text{HI}}}{c} \right], \quad (9)$$

where $\hat{\mathbf{k}}_i$ and $\hat{\mathbf{k}}_f$ are unit wavevectors associated with the incident and outgoing Rayleigh-scattered photons, and \mathbf{v}_{HI} is the velocity of the hydrogen atom in the observer's rest frame. From this relation, a Rayleigh-reflected photon from a hydrogen atom moving with a speed $v_{\text{HI}} = 40 \text{ km s}^{-1}$ will acquire a Doppler factor of 80 km s^{-1} , and subsequent Raman scattering will result in a redshifted optical photon with $\Delta V \sim 400 \text{ km s}^{-1}$ from the atomic line center of Raman-scattered He II. Several Rayleigh reflections are sufficient to achieve a wavelength shift to reach H I Ly γ resonance to emit a H β line photon as a result of final Raman scattering. In this particular case, Raman conversion efficiency becomes significantly enhanced because of the enormous cross section at resonance.

2.2. Scattering Geometry

A near-IR emission line at $2 \mu\text{m}$ of H $_2$ was found in the PN NGC 7027 by Treffers et al. (1976). Detection of molecular emission from PNe strongly implies that the circumnebular region is ionization bounded rather than matter bounded (Dinerstein 1991). Circumnebular neutral hydrogen H I has been detected in several young PNe through 21 cm radio observation. Taylor et al. (1989) carried out 21 cm observations of the pPN IC 418 using the Very Large Array (VLA) to detect an absorption feature that is due to the expanding nebula and an emission consistent with a total H I mass $\sim 0.07 M_\odot$ assuming a spin excitation temperature of $\sim 10^3 \text{ K}$.

Figure 2 is a schematic illustration of the scattering geometry considered in this work. The He II emission source is located at the center, surrounded by a neutral spherical shell with inner and outer radii R_i and R_o , respectively. We assume that the spherical shell moves radially outward with a single speed v_{exp} in such a way that the mass flux is conserved at each radial coordinate r . That is, the H I number density $n_{\text{H}}(r)$ is given by

$$\begin{aligned} n_{\text{HI}}(r) &= \frac{\dot{M}}{4\pi r^2 \mu_a m_p v_{\text{exp}}} \\ &= 1.34 \times 10^5 \text{ cm}^{-3} \left(\frac{\dot{M}}{10^{-5} M_\odot \text{ yr}^{-1}} \right) \\ &\quad \times \left(\frac{r}{10^3 \text{ au}} \right)^{-2} \left(\frac{v_{\text{exp}}}{10 \text{ km s}^{-1}} \right)^{-1} \end{aligned} \quad (10)$$

where \dot{M} is the mass-loss rate and μ_a is the mean molecular weight. For simplicity, we set $\mu_a = 1$ assuming that the scattering region purely consists of atomic hydrogen.

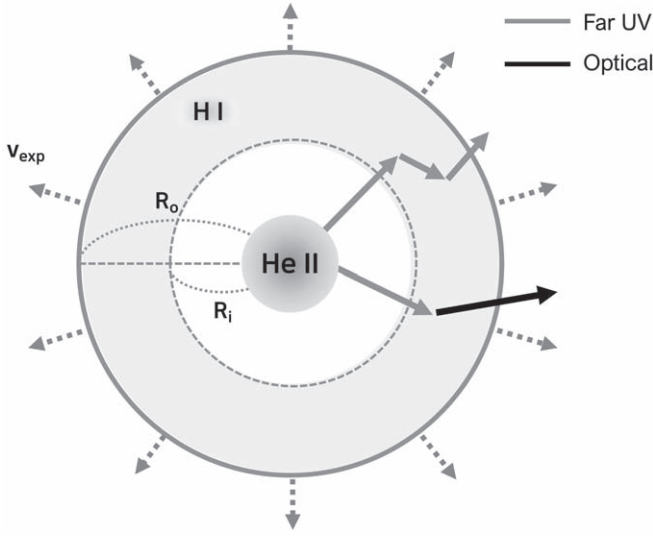


Figure 2. Schematic illustration of the simulation geometry. The H I region is assumed to be a spherical shell with inner and outer radii of R_i and R_o , respectively. A point-like He II emission source is located at the center. The scattering region expands radially from the He II source with a constant velocity v_{exp} . He II photons may escape through either Rayleigh or Raman scattering. The black arrow shows an escaping optical Raman photon, whereas the gray arrows represent paths traversed by Rayleigh-scattered far-UV photons.

We measure the H I column density N_{HI} of the H I shell along the radial direction so that

$$N_{\text{HI}} = \int_{R_i}^{R_o} n_{\text{HI}}(r) dr N_{\text{HI},0} \left(1 - \frac{R_i}{R_o}\right). \quad (11)$$

Here, the characteristic H I column density can be expressed as

$$N_{\text{HI},0} = 2 \times 10^{21} \dot{M}_{-5} r_{-3}^{-2} v_{\text{exp},10}^{-1} \text{ cm}^{-2}, \quad (12)$$

in terms of dimensionless quantities $\dot{M}_{-5} = \dot{M}/(10^{-5} M_{\odot} \text{ yr}^{-1})$, $r_{-3} = r/(10^3 \text{ au})$, and $v_{\text{exp},10} = v_{\text{exp}}/(10 \text{ km s}^{-1})$. The H I mass of the neutral shell is given by

$$M_{\text{HI}} = (5 \times 10^{-3} M_{\odot}) \dot{M}_{-5} v_{\text{exp},10}^{-1} \left(\frac{R_o}{10^3 \text{ au}}\right) \left(1 - \frac{R_i}{R_o}\right). \quad (13)$$

In this work, we assume that the He II emission source is unpolarized and isotropic in order to focus on the basic physics of line profile formation. We consider two cases: in the first, the He II emission source is monochromatic at the line center, and in the second case, the emission line profile is described by a Gaussian function.

2.3. Grid-based Monte Carlo Approach

In order to describe Rayleigh and Raman scattering in an expanding neutral medium, a new grid-based Monte Carlo code was developed, where a Cartesian coordinate system is adopted and the scattering region is divided into a large number of cubes of equal size. The He II line source is located at the center of the coordinate system, and uniform physical properties such as H I number density n_I and velocity \mathbf{v}_I are assigned to each cube I with the center coordinate (x_i, y_j, z_k) .

For cube I with radial distance $r = (x_i^2 + y_j^2 + z_k^2)^{1/2}$, the H I number density n_I is given by Equation (10) if $R_i < r < R_o$. Otherwise, we set $n_I = 0$. The expanding velocity of cube I is

also given by

$$\mathbf{v}_I = v_{\text{exp}} \frac{x_i \hat{\mathbf{x}} + y_j \hat{\mathbf{y}} + z_k \hat{\mathbf{z}}}{r}, \quad (14)$$

in accordance with our assumption of spherical inertial expansion.

Now we consider a He II $\lambda 972$ photon propagating from a starting point \mathbf{r}_p with a unit wavevector $\hat{\mathbf{k}}$. We determine all of the nonempty cubes that lie along the semi-infinite ray starting at \mathbf{r}_p in the direction $\hat{\mathbf{k}}$. Labeling these cubes with subscript I , we compute the scattering optical depth τ_I corresponding to the photon path inside cube I between the entering and exiting points. In the rest frame of cube I , the He II photon is treated as monochromatic with frequency

$$\omega_I = \omega_0 (1 + \mathbf{v}_I \cdot \hat{\mathbf{k}}/c), \quad (15)$$

where $\hat{\mathbf{k}}$ is the unit wavevector of the photon. Using this frequency, we obtain an appropriate cross section $\sigma_{\text{tot}}(\omega_I)$. With this cross section, the scattering optical depth τ_I is given by

$$\tau_I = n_I \sigma_{\text{tot}}(\omega_I) l_I, \quad (16)$$

where l_I is the path length through the cube. By summing all τ_I , we obtain τ_{∞} , the scattering optical depth to an observer at infinity.

A line photon is supposed to traverse a physical distance l that corresponds to an optical depth τ given by

$$\tau = -\ln r_p, \quad (17)$$

where r_p is a uniform random deviate in the range between 0 and 1. If $\tau > \tau_{\infty}$, then the line photon passes through the neutral region and reaches the observer as a far-UV He II $\lambda 972$ photon. Otherwise, the photon is scattered at some cube J , where the cumulative optical depth τ_I just exceeds τ . Linearly interpolating the optical depths at the entering and exiting points of cube J , we determine the scattering site inside cube J .

In this work, the geometry is spherically symmetric, so no consideration is given to polarization. According to Stenflo (1980), the probabilistic angular distribution of the scattered radiation for Rayleigh and Raman scattering with atomic hydrogen sufficiently far from resonance is identical to that for Thomson scattering, which is given as

$$f(\beta) \propto (1 + \beta^2). \quad (18)$$

Here, β is the cosine of the angle between the incident and scattered photons.

At the scattering site, the wavevector is chosen according to the scattering phase function, and the scattering type is also determined in accordance with the branching ratios b_{r1} , b_{r2} , and $b_{r3} = 1 - b_{r1} - b_{r2}$ with b_{ri} branching ratios for scattering into $n = 1$, $n = 2$, and $n = 3$ levels, respectively.

We regard the neutral shell as optically thin to optical photons, such that Raman-scattered photons escape from the region without any further interaction. If the scattering is Rayleigh, the procedure is repeated until the far-UV He II photon escapes either as a Raman-scattered optical photon or as a Rayleigh-scattered He II photon when $\tau > \tau_{\infty}$.

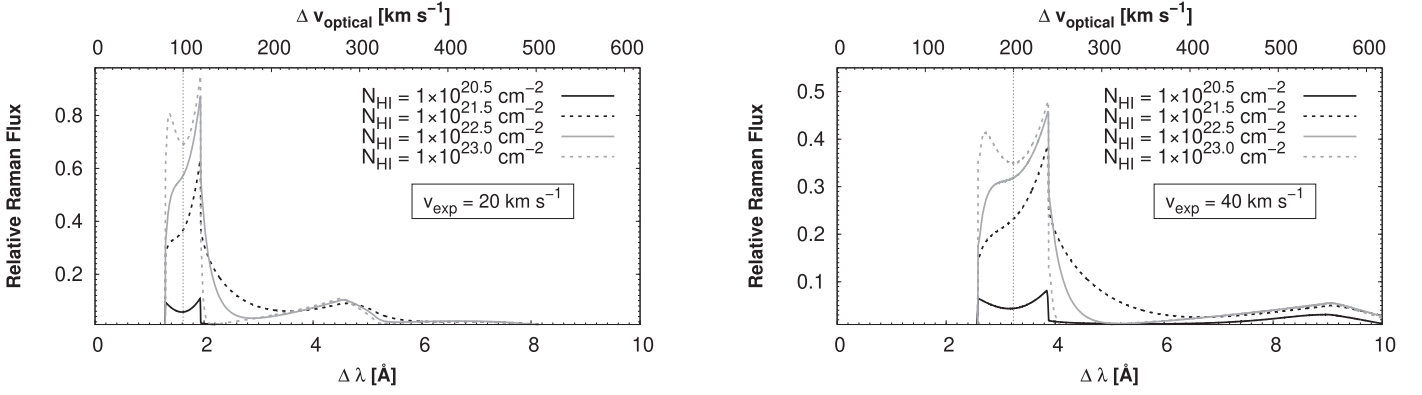


Figure 3. Line profiles of Raman He II $\lambda 4851$ obtained from our Monte Carlo simulations for various column densities with two values $v_{\text{exp}} = 20$ (left panel) and 40 km s^{-1} (right panel) of the expansion speed of the spherical neutral shell. The horizontal axis represents the wavelength shift from the Raman He II line center in units of \AA (lower axis) and km s^{-1} with respect to the optical Raman-scattered line center (upper axis). The vertical dotted line in each panel marks the wavelength shift that corresponds to v_{exp} .

3. Results

3.1. Monochromatic Source

In Figure 3, we show the resultant profiles of Raman-scattered He II $\lambda 4851$ formed in an expanding spherical H I shell surrounding a monochromatic point-like He II emission source located at the center of the shell. We consider various values N_{HI} of H I column density ranging from $10^{20.5}$ to 10^{23} cm^{-2} . The left and right panels of Figure 3 correspond to the cases of the expansion velocity $v_{\text{exp}} = 20 \text{ km s}^{-1}$ and 40 km s^{-1} , respectively.

The lower horizontal axis shows the wavelength shift $\Delta\lambda$ from the atomic line center $\lambda_{c,4851}$ of Raman He II $\lambda 4851$ in units of \AA . The upper horizontal axis shows the apparent Doppler factor ΔV in units of km s^{-1} , which is related to the wavelength shift $\Delta\lambda$ by

$$\frac{\Delta V}{c} = \left(\frac{\lambda_0}{\lambda_l} \right) \frac{\Delta\lambda}{\lambda_0}. \quad (19)$$

It should be noticed that the apparent Doppler factor ΔV approximately corresponds to the relative speed of H I and He II multiplied by a factor of 5. The vertical dotted line in each panel marks the center of the Raman feature located at $\Delta V_c = (\lambda_0/\lambda_l)v_{\text{exp}}$, which is ~ 100 and 200 km s^{-1} for $v_{\text{exp}} = 20$ and 40 km s^{-1} . In this article, we call the center wavelength λ_c corresponding to ΔV_c the ‘‘Raman line center.’’

A spherical shell with $N_{\text{HI}} = 10^{20.5} \text{ cm}^{-2}$ expanding with $v_{\text{exp}} < 100 \text{ km s}^{-1}$ is optically thin for both Rayleigh and Raman scattering, and therefore resultant profiles are double peaked, consisting of two peaks of similar strength. It is also notable that a faint extended red tail appears. In this case, a significant fraction of incident far-UV photons penetrate the H I region with no interaction or escape the scattering region after a single Rayleigh scattering, leading to formation of a very weak Raman feature. The Raman feature is contributed dominantly by singly Rayleigh-scattered radiation. Since the phase function for Rayleigh and Raman scattering sufficiently far from resonance is symmetric with respect to the incidence direction, forward and backward scatterings are equally probable, resulting in an almost symmetric double-peak structure with blue and red peaks located at $\Delta V_b = \Delta V_c - v_{\text{exp}}$ and $\Delta V_r = \Delta V_c + v_{\text{exp}}$, respectively.

As N_{HI} is increased to $N_{\text{HI}} \sim 10^{22} \text{ cm}^{-2}$, the blue peak becomes significantly weaker relative to the red counterpart, accompanied by the enhancement of the red extended tail. When a He II $\lambda 972$ line photon is Rayleigh scattered in an expanding H I region, it is redshifted in the rest frame of the scattering hydrogen atom. Because the Rayleigh scattering cross section increases sharply as a function of wavelength, the expanding neutral medium becomes moderately optically thick with respect to Rayleigh scattering. Several Rayleigh scatterings before a final Raman scattering provide a sufficient redward push in wavelength space, leading to frequency redistribution from the blue peak to the extended red tail.

However, in the case at very high H I column density, $N_{\text{HI}} \geq 10^{22.5} \text{ cm}^{-2}$, the scattering region is optically thick to most He II $\lambda 972$ line photons for which Rayleigh scattering is effectively local, due to the short mean free path. Therefore, redward diffusion in wavelength space is severely restricted because of the small velocity difference in a localized region. Consequently, considerably symmetric double-peak profiles are restored in a neutral region with very high N_{HI} , which is shown in Figure 3.

A similar behavior is also found in the profiles shown in the right panel of Figure 3, for which $v_{\text{exp}} = 40 \text{ km s}^{-1}$. Because v_{exp} is twice that for the left panel, the Doppler factor ΔV_c for the ‘‘Raman line center’’ and the width of the main double-peak part are twice the counterparts shown in the left panel. In addition, because the scattering cross section is higher for large λ , the total Raman flux integrated over the entire wavelength interval is stronger than the counterpart in the left panel with the same N_{HI} .

In Figure 4, we illustrate schematically how the main double peaks and the extended red part are formed. In panel (a), we show a singly scattered photon, where a forward-moving Raman optical photon is detected by the observer as a photon constituting the main blue peak with the Doppler factor ΔV_b corresponding to v_{exp} from the Raman line center. On the other hand, a backward-moving Raman photon falls on the main red peak with the wavelength corresponding to $-v_{\text{exp}}$ from the Raman line center. In the optically thin limit, due to symmetry between forward and backward scattering, we obtain a symmetric double-peak profile.

Panel (b) illustrates a case for an initially forward Rayleigh-scattered photon followed by a few local Rayleigh scatterings. In this case, frequency diffusion is severely limited because of

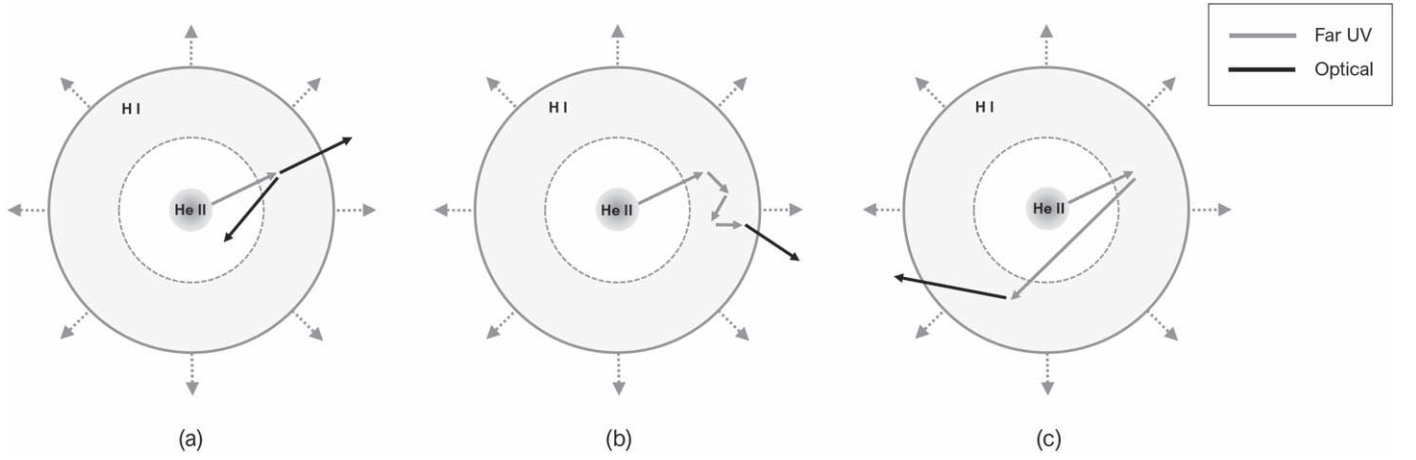


Figure 4. Schematic illustration showing the formation of the double-peak profile with an extended tail structure. The gray arrows indicate the path of far-UV photons that are emitted from the central He II source and subsequently Rayleigh scattered. The black arrows correspond to Raman-scattered optical He II photons. (a) An escaping Raman photon is blueshifted for a forward final scattering, and a redshifted photon is obtained from a backward scattering. (b) Local Rayleigh scattering results in only slight frequency diffusion. (c) A Rayleigh reflection leads to significant wavelength increase, leading to formation of an extended red part.

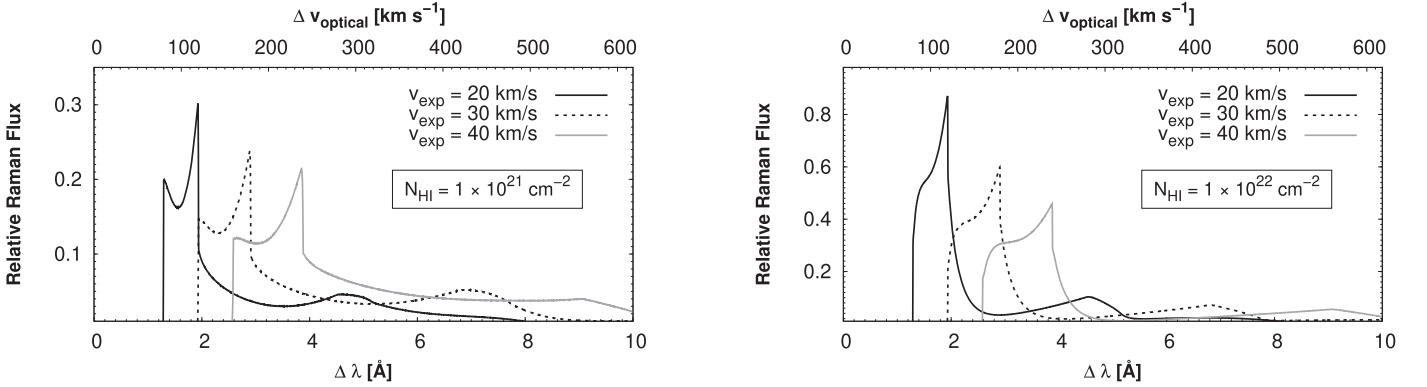


Figure 5. Line profiles of Raman He II $\lambda 4851$ obtained from our Monte Carlo simulations for various values of the expansion speed v_{exp} . The left and right panels show line profiles obtained for $N_{\text{H I}} = 10^{21}$ and 10^{22} cm^{-2} . The horizontal and vertical axes are the same as in Figure 3.

the local nature of scattering. This shows that in a highly optically thick case, double-peak profiles are restored. However, as shown in panel (c), Rayleigh reflection at the inner surface may produce significant redshift, leading to formation of an extended red tail structure.

In Figure 5, we present our simulated Raman He II profiles for the values 20, 30, and 40 km s^{-1} of the expansion speed v_{exp} and for two fixed values $N_{\text{H I}} = 10^{21}$ and 10^{22} cm^{-2} of H I column density. The resultant profiles exhibit a very asymmetric double-peak structure with a tertiary peak in an extended red tail. The center wavelength of Raman-scattered He II shifts redward as v_{exp} increases. Furthermore, because the cross section increases sharply toward H I resonance, the line flux of Raman-scattered He II also increases. As we mentioned, the enhancement of red peaks and the formation of a tertiary peak are attributed to multiple Rayleigh scattering events before escape as an optical Raman photon. The tertiary peaks in the extended red tail region appear at $\Delta V = 300, 450,$ and 600 km s^{-1} for $v_{\text{exp}} = 20, 30,$ and 40 km s^{-1} , respectively. The tertiary peaks are constituted mostly by twice Rayleigh reflected photons at the inner surface at $r = R_i$, first at the part moving toward the observer and second at the part moving away from the observer.

In Figure 6, we plot the Raman conversion efficiency, defined as the photon number ratio of incident He II $\lambda 972$ and the Raman-scattered spectral line. For He II $\lambda 972$, there are two

Raman scattering channels, one corresponding to final deexcitation into the $2s$ state and the other $3s$ and $3d$ states. Because in this work we only focus on line formation for Raman scattering into the $2s$ state, we first compute the Raman conversion efficiency R_{2s} , defined as

$$R_{2s} = \frac{\Phi_{2s}}{\Phi_{\text{He II } 972}}, \quad (20)$$

where $\Phi_{\text{He II } 972}$ and Φ_{2s} are the number fluxes of Raman-scattered He II $\lambda 4851$ and far-UV He II $\lambda 972$, respectively. In an analogous way, we define the Raman conversion efficiency R_{3s3d} as

$$R_{3s3d} = \frac{\Phi_{3s3d}}{\Phi_{\text{He II } 972}}, \quad (21)$$

where Φ_{3s3d} is the number flux of Raman-scattered IR photons as a result of final deexcitation into $3s$ or $3d$ states.

In the left panel of Figure 6, we show the total Raman conversion efficiency R_{tot} , defined as the sum of R_{2s} and R_{3s3d} . As is found in the left panel, the total Raman conversion efficiency R_{tot} increases to unity as either $N_{\text{H I}}$ or v_{exp} increases. As v_{exp} increases, He II $\lambda 972$ line photons are redshifted toward Ly γ in the rest frame of a hydrogen atom, resulting in a dramatic increase in scattering cross section and a sharp rise in

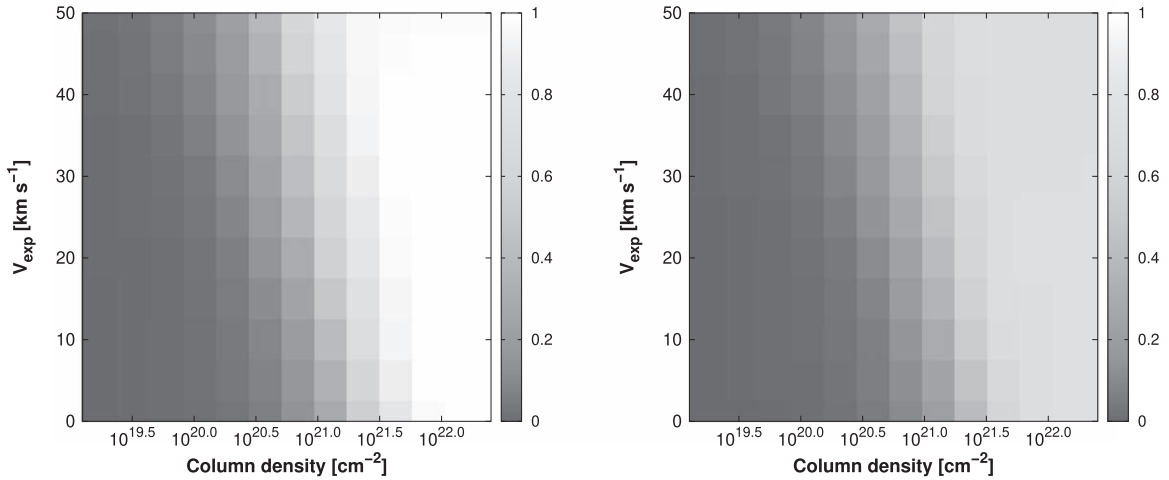


Figure 6. Raman conversion efficiency for various values of v_{exp} and N_{HI} . The left panel shows the total Raman conversion efficiency R_{tot} for He II $\lambda 972$, defined as the sum of R_{2s} and R_{3s3d} , the Raman conversion efficiencies into the $2s$ state and the $3s$ and $3d$ states, respectively. The right panel shows the Raman conversion efficiency R_{2s} . Note that the numerical results shown in the bottom of both panels correspond to the case of a static H I medium.

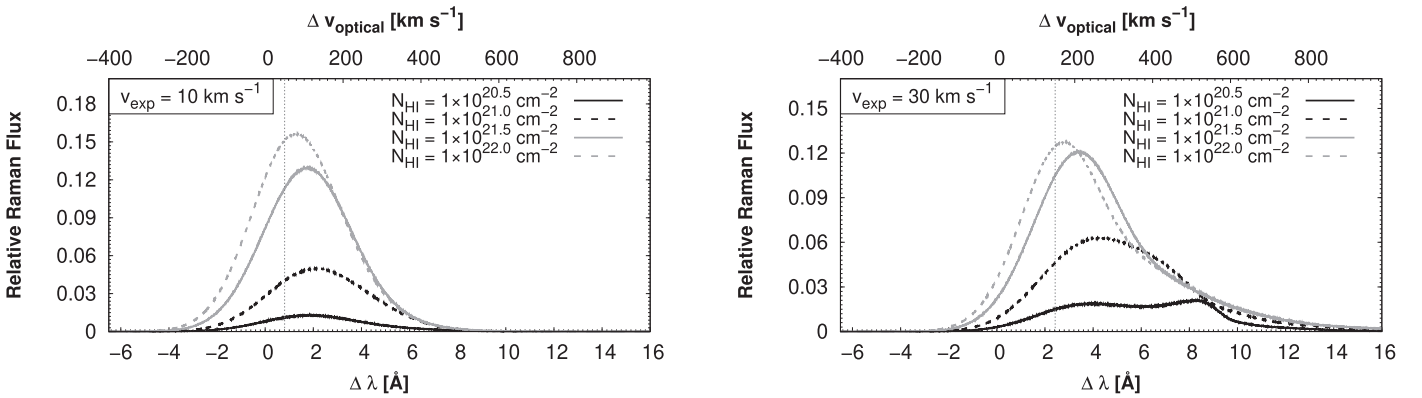


Figure 7. Line profiles of Raman-scattered He II formed in an expanding spherical, neutral shell illuminated by a point-like He II line source with a Gaussian line profile with the FWHM of $\Delta v_G = 50 \text{ km s}^{-1}$. The left panel shows the resultant profiles for an expansion speed $v_{\text{exp}} = 10 \text{ km s}^{-1}$ and four values of N_{HI} . The right panel is for $v_{\text{exp}} = 30 \text{ km s}^{-1}$.

Raman conversion efficiency. The Raman scattering optical depth also increases by simply increasing N_{HI} .

Specifically, we obtain the Raman conversion efficiencies $R_{2s} = 0.16$ and $R_{3s3d} = 0.06$ for the case of a stationary H I region with H I column density $N_{\text{HI}} = 10^{21} \text{ cm}^{-2}$. This implies that 78% of far-UV He II escape through Rayleigh scattering or without interaction. In contrast, in the case of an expanding neutral region with $v_{\text{exp}} = 20 \text{ km s}^{-1}$ and the same N_{HI} , we obtain $R_{2s} = 0.34$ and $R_{3s3d} = 0.12$. The efficiencies increase to $R_{2s} = 0.51$ and $R_{3s3d} = 0.18$ for an expanding neutral region with a speed of 40 km s^{-1} .

The right panel of Figure 6 shows the Raman conversion efficiency R_{2s} giving the fraction of Raman-scattered He II $\lambda 4851$ only. The highest value that R_{2s} may reach in the optically thick limit is shown to be ~ 0.8 , which is found in the top right portion of the figure. On the other hand, in the opposite limit of low optical depth, the fraction R_{2s} is ~ 0.1 , which is the quantum mechanical branching ratio for single scattering.

3.2. Gaussian Source

With the assumption that the He II emission source is isotropic and that the case B recombination is valid, we may safely infer the line profile of far-UV He II $\lambda 972$ by investigating optical He II

emission lines such as He II $\lambda 4686$ and He II $\lambda 4859$ (Hummer & Storey 1987). However, it should be noted that the validity of this assumption is questionable when a He II emission region has an orderly motion, such as rotation in a specified plane that coincides with the binary orbital plane or perpendicular to the symmetry axis along which bipolar nebular morphology develops.

Jung & Lee (2004) performed a profile analysis of He II $\lambda 4859$ and H β of the symbiotic star V1016 Cygni. They reported that H β and He II $\lambda 4859$ are fitted well using a single Gaussian function with an FWHM of $\Delta v_G = 77 \text{ km s}^{-1}$. Considering that He II is four times heavier in atomic weight than hydrogen, the emission line profiles are attributed to the convolution of thermal and turbulent motions. A similar study of the PN IC 5117 conducted by Lee et al. (2006) shows that H β and He II $\lambda 4859$ are also well fitted by a single Gaussian function with FWHM of $\Delta v_G = 43$ and 35 km s^{-1} , respectively. It appears that the profile widths of H β and He II are significantly contributed by dynamical motions in addition to thermal motions.

In Figure 7, we show the line profiles of Raman-scattered He II, where the He II emission source is at the center with a Gaussian line profile with the FWHM $\Delta v_G = 50 \text{ km s}^{-1}$. In the left panel, we show our result for an expansion speed $v_{\text{exp}} = 10 \text{ km s}^{-1}$, and the right panel shows the result for

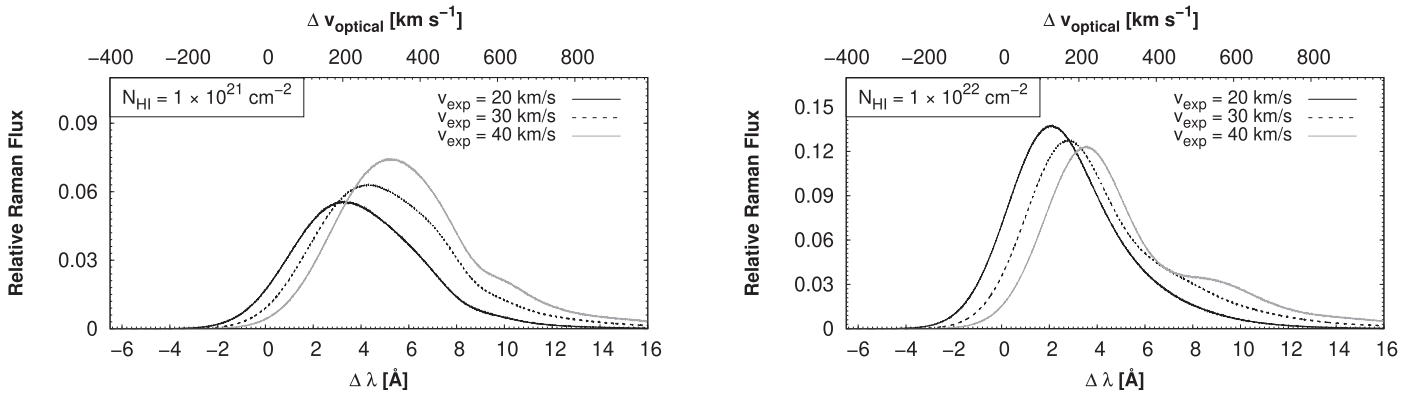


Figure 8. Same result as Figure 7 but for various values of v_{exp} . The left panel shows the resultant profiles for $N_{\text{H I}} = 10^{21} \text{ cm}^{-2}$ and three values of v_{exp} . The right panel is for 10^{22} cm^{-2} .

$v_{\text{exp}} = 30 \text{ km s}^{-1}$. The dashed vertical line represents the wavelength at which a line-center He II photon is Raman scattered by a hydrogen atom moving away with v_{exp} . The lower horizontal axis shows the wavelength shift measured from $\lambda_{c,4851}$ as defined in Equation (5).

In the left panel, we find that the line profiles are slightly distorted redward because of a sharp increase of Raman cross section. In the right panel, we find more severe profile distortion, which is attributed to the increased range of cross section variation. Multiply Rayleigh-scattered photons significantly contribute to the emergent flux in the red part in a complicated way.

In the case of $v_{\text{exp}} = 10 \text{ km s}^{-1}$, the ‘‘Raman line center’’ represented by the dashed vertical line is found at $\Delta\lambda = 0.81 \text{ \AA}$. The profile peaks are formed at $\Delta\lambda = 1.83, 2.00, 1.79,$ and 1.22 \AA for $N_{\text{H I}} = 10^{20.5}, 10^{21}, 10^{21.5},$ and 10^{22} cm^{-2} , respectively. It should be noted that the peak position $\Delta\lambda$ varies with $N_{\text{H I}}$ in a nonmonotonic way (Jung & Lee 2004).

On the other hand, the ‘‘Raman line center’’ is found at $\Delta\lambda = 2.43 \text{ \AA}$ in the right panel, where $v_{\text{exp}} = 30 \text{ km s}^{-1}$. We find that the peaks are located at $\Delta\lambda = 4.23, 3.44,$ and 2.83 \AA for $N_{\text{H I}} = 10^{21}, 10^{21.5},$ and 10^{22} cm^{-2} . In the case of $N_{\text{H I}} = 10^{20.5} \text{ cm}^{-2}$, a conspicuous red peak at $\Delta\lambda = 8.36 \text{ \AA}$ appears in addition to a peak at $\Delta\lambda = 4.12 \text{ \AA}$.

In Figure 8, we present the line profile of Raman-scattered He II with the same emission source for a fixed value of $N_{\text{H I}} = 10^{21} \text{ cm}^{-2}$ and $N_{\text{H I}} = 10^{22} \text{ cm}^{-2}$ in the left and right panels, respectively. In the left panel, profile peaks are found at $\Delta\lambda = 3.23, 4.23,$ and 5.29 \AA for $v_{\text{exp}} = 20, 30,$ and 40 km s^{-1} . In the right panel with $N_{\text{H I}} = 10^{22} \text{ cm}^{-2}$, we find that $\Delta\lambda = 2.04, 2.83,$ and 3.52 \AA for the same values of v_{exp} as in the left panel. We note that the peaks are not equally spaced and that the line profiles are significantly skewed, showing redward enhancement. This indicates that great caution should be exercised in the determination of the expansion speed from observed Raman-scattered He II features.

We also investigate the dependence of Δv_{G} and show additional results for $\Delta v_{\text{G}} = 30$ and 70 km s^{-1} in Figures 9 and 10. We show the results for various values of $N_{\text{H I}}$ in Figure 9. In addition, Figure 10 shows the results for various values of v_{exp} . The left panels of Figures 9 and 10 are for $\Delta v_{\text{G}} = 30 \text{ km s}^{-1}$, and the right panels show the results for $\Delta v_{\text{G}} = 70 \text{ km s}^{-1}$. In the top panels of Figure 9 with $v_{\text{exp}} = 10 \text{ km s}^{-1}$, we find that all of the line profiles are singly peaked with redward asymmetry. The nonmonotonic behavior of the peak positions is

similar to that found in the case of $\Delta v_{\text{G}} = 50 \text{ km s}^{-1}$ as discussed in Section 3.2. For $\Delta v_{\text{G}} = 70 \text{ km s}^{-1}$ and $N_{\text{H I}} = 10^{21} \text{ cm}^{-2}$, the peak position is quite significantly redshifted, and the line profile is conspicuously distorted.

In the bottom left panel of Figure 9 with $v_{\text{exp}} = 30 \text{ km s}^{-1}$, additional red peaks are found. An incident He II photon acquires a Doppler factor corresponding to $\sim 3v_{\text{exp}}$ as a result of double Rayleigh reflections in the spherical shell, which leads to the formation of the additional red peaks. Because of the increased cross section for redshifted photons, the profile distortion is quite conspicuous for $N_{\text{H I}} = 10^{20.5} \text{ cm}^{-2}$.

In the bottom right panel of Figure 9, the resultant line profiles are singly peaked but with large redward skewness. This result indicates that peak position may move substantially redward for broad He II because line photons are distributed up to the blue vicinity of Ly γ resonance. In the case of $v_{\text{exp}} = 30 \text{ km s}^{-1}$, $\Delta v_{\text{G}} = 70 \text{ km s}^{-1}$, and $N_{\text{H I}} = 10^{21} \text{ cm}^{-2}$, the profile peak is found at $\Delta\lambda = 5.54 \text{ \AA}$, which corresponds to $+343 \text{ km s}^{-1}$ in optical velocity space. It gives an expansion speed of the neutral medium of about $v_{\text{exp}} = 78 \text{ km s}^{-1}$ with a simple single Gaussian profile fitting. For $N_{\text{H I}} \leq 10^{21} \text{ cm}^{-2}$, the profile peaks are found at Doppler factors two or three times larger than that for $v_{\text{exp}} = 30 \text{ km s}^{-1}$. This corroborates our conclusion that v_{exp} should not be deduced from the peak position alone.

In the top left panel of Figure 10 for which $N_{\text{H I}} = 10^{21} \text{ cm}^{-2}$, we observe the development of red shoulder features that are formed by Rayleigh reflections at the inner surface of the H I shell. As v_{exp} increases, the peak positions move redward, which is accompanied by enhancement of the Raman conversion efficiency. This indicates very clearly that the Raman conversion efficiency is affected by the kinematics as well as the H I column density and covering factor.

A similar behavior can be noticed in the top right panel, where the peak positions appear at larger $\Delta\lambda$ than those in the left panel. It should be noticed that even the peak positions are severely affected by the profile of the He II emission source located at the center of the spherical H I shell.

In the bottom panels of Figure 10 for which $N_{\text{H I}} = 10^{22} \text{ cm}^{-2}$, the development of an extended red tail part is severely suppressed compared to the case shown in the top panels. The line flux of Raman-scattered He II is concentrated near the main peak formed at $\Delta\lambda$ that corresponds to v_{exp} . This is explained by the local nature of Rayleigh scattering, which takes place near the entry spot in a scattering region with a

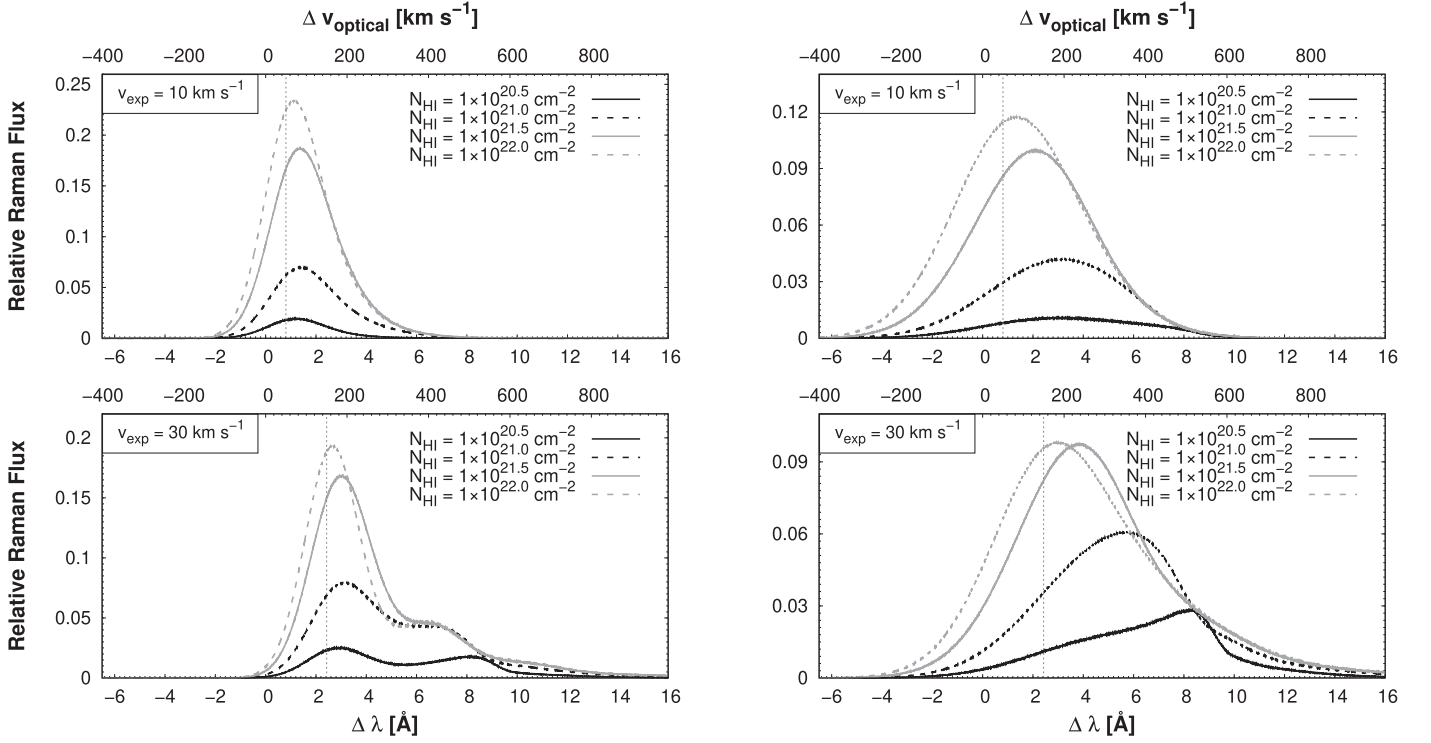


Figure 9. Line profiles of Raman-scattered He II formed in an expanding spherical, neutral shell with a point-like He II source with a Gaussian line profile of which the FWHM $\Delta v_G = 30 \text{ km s}^{-1}$ (left) and 70 km s^{-1} (right). The upper panel shows the resultant profiles for an expansion speed $v_{\text{exp}} = 10 \text{ km s}^{-1}$ with four values of $N_{\text{H I}}$. The lower panel is for $v_{\text{exp}} = 30 \text{ km s}^{-1}$.

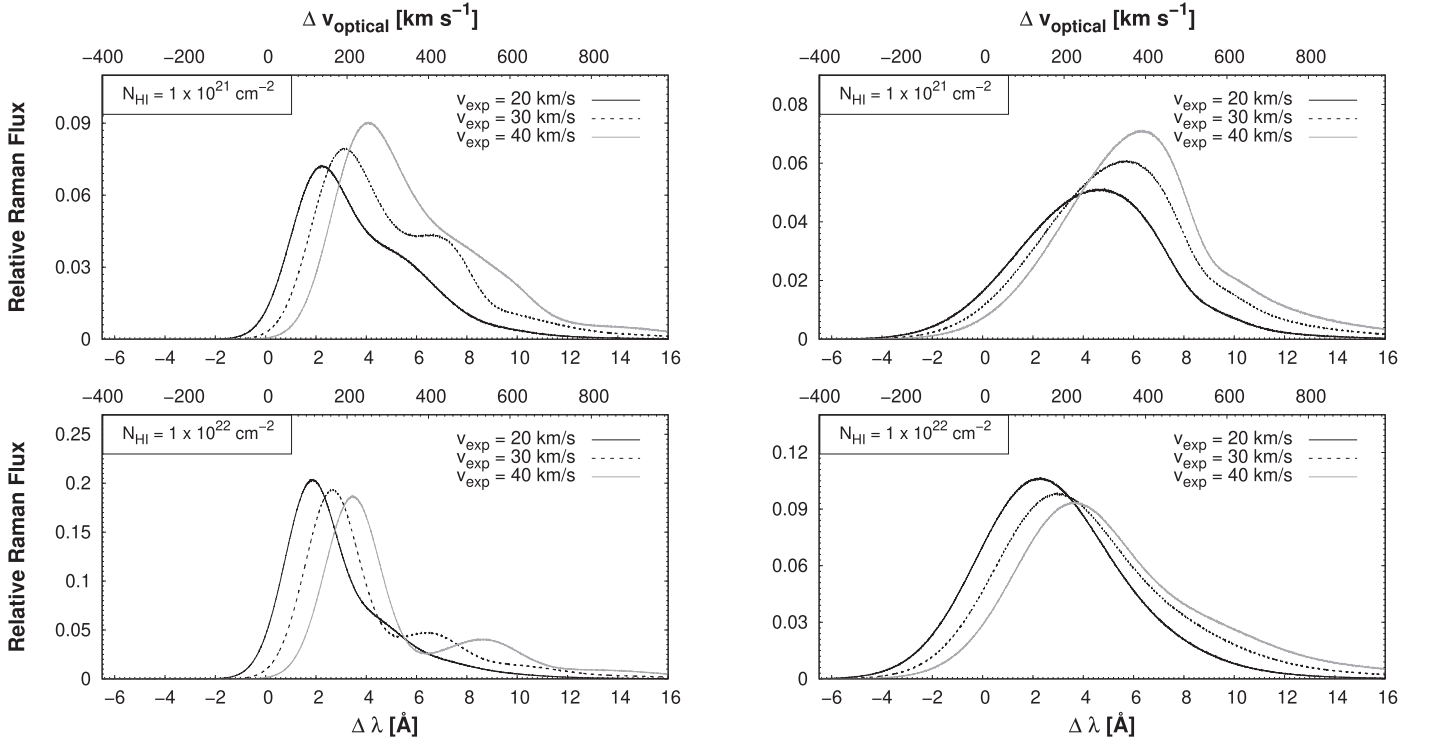


Figure 10. Line profiles of Raman-scattered He II formed in an expanding spherical, neutral shell with a point-like He II source with a Gaussian line profile of which the FWHM $\Delta v_G = 30 \text{ km s}^{-1}$ (left) and 70 km s^{-1} (right). The upper panel shows the resultant profiles for column density $N_{\text{H I}} = 10^{21} \text{ cm}^{-2}$ with three values of expansion speed v_{exp} . The lower panel is for $N_{\text{H I}} = 10^{22} \text{ cm}^{-2}$.

large scattering optical depth. Only a small fraction of line photons make a substantial excursion by Rayleigh reflection, constituting the extended red part.

In the bottom left panel, Rayleigh-reflected He II photons form a relatively weak red peak at $(2-3) \times v_{\text{exp}}$. However, in the right panels, the overall line profiles are singly peaked with

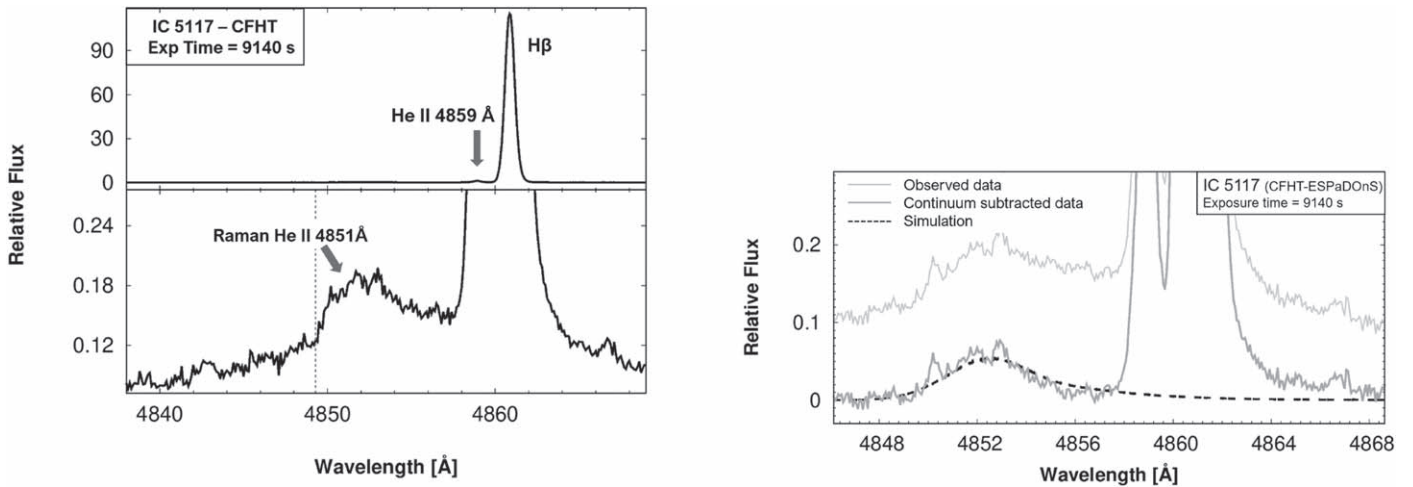


Figure 11. CFHT spectrum of IC 5117 around H β (left) and our Monte Carlo profile fit (right). He II λ 4859 is seen blueward of H β in the upper left panel. The lower panel is a blown-up version of the upper panel in order to clearly present the very weak Raman-scattered He II λ 4851 appearing as a broad emission feature blueward of He II λ 4859. The right panel shows continuum-subtracted data and the best fit with simulated data obtained with $v_{\text{exp}} = 30 \text{ km s}^{-1}$ and $N_{\text{H I}} = 10^{21} \text{ cm}^{-2}$.

Table 1
Single Gaussian Parameters for Observational Data of IC 5117

Line	λ_0 (Å)	$\Delta\lambda$ (Å)	f_0
H β λ 4861	4860.879	0.668	110.54
He II λ 4859	4858.942	0.573	1
Raman He II λ 4851	4852.055	3.424	0.056

a rather smooth, extended tail in the red part. One may also notice that the overall Raman conversion efficiency reaches the theoretical maximum value ~ 0.8 and is quite independent of v_{exp} . Due to suppression of development in the red part, the peak positions faithfully represent the values of v_{exp} .

3.3. Application to the Young PN IC 5117

In the left panels of Figure 11, we present a part of the spectrum showing the Raman He II λ 4851 and H β of IC 5117 observed with ESPaDOnS (Echelle Spectropolarimetric Device for the Observation of Stars) installed on the Canada–France–Hawaii Telescope (CFHT). The observation was carried out on the two nights of 2014 September 6 and 14, and the total exposure time is 9140 s. The lower left panel is a blown-up version of the upper panel, in which the Raman-scattered He II feature appears clearly as a broad emission feature blueward of He II λ 4859. The dashed vertical line marks the “Raman line center” of Raman He II λ 4851, which is expected to appear based on the pure atomic physics relation given by Equation (4).

The line profiles of H β , He II λ 4859, and Raman-scattered He II λ 4851 are analyzed using a single Gaussian function,

$$f(\lambda) = f_0 \exp\left(-\frac{(\lambda - \lambda_0)^2}{2\Delta\lambda^2}\right), \quad (22)$$

where the fitting parameters are presented in Table 1. The line flux ratio of Raman He II and He II was 0.081 in the previous study of IC 5117 observed in 2004 by Lee et al. (2006), which is different from the value 0.056 presented in Table 1. However, this difference is partly due to the poor quality of the 2004 data and partly to the ambiguity of continuum subtraction around weak and broad Raman He II.

The line center of Raman He II is observed at 4852.06 Å, which is redward of the value expected from atomic physics by about 2.43 Å. This may indicate the H I region expanding with a speed of 30 km s⁻¹. The Raman conversion efficiency R_{2s} is calculated with the same method adopted by Lee et al. (2006) by assuming the validity of the case B recombination theory for He II (e.g., Storey & Hummer 1995). From the definition of R_{2s} given in Equation (20), we have

$$R_{2s} \equiv \frac{\Phi_{2s}}{\Phi_{\text{He II } 972}} = \frac{F_{4851}/h\nu_{4851}}{F_{972}/h\nu_{972}} = \left(\frac{F_{4851}/h\nu_{4851}}{F_{4859}/h\nu_{4859}}\right) \left(\frac{F_{4859}/h\nu_{4859}}{F_{972}/h\nu_{972}}\right), \quad (23)$$

where F_{4851} is the total line flux of Raman He II λ 4851, and other total He II emission line fluxes are defined in a way similar to that adopted by Lee et al. (2006). The ratio of the photon number fluxes Φ_{4851}/Φ_{4859} is measured to be 0.33. Assuming the electron temperature $T_e = 2 \times 10^4$ K and the electron density $n_e = 10^4 \text{ cm}^{-3}$, the case B recombination theory yields the ratio of the photon number fluxes $\Phi_{4859}/\Phi_{972} = 1.046$, which finally leads to $R_{2s} = 0.34$.

In the right panel of Figure 11, we present our profile fit shown as a dashed line. The adopted model parameters are $\Delta v_G = 35 \text{ km s}^{-1}$, $N_{\text{H I}} = 10^{21} \text{ cm}^{-2}$, and $v_{\text{exp}} = 30 \text{ km s}^{-1}$. The overall agreement is acceptable, but it should be noted that the data are of insufficient quality.

This expansion speed is larger than the value of 21 km s⁻¹ suggested by Weinberger (1989), who used [N II] lines. Gussie & Taylor (1995) used the VLA to propose that the CO component is expanding with a speed of 17 km s⁻¹. The discrepancy in expansion speeds between our result and that of other researchers may result from our adoption of a very simple scattering geometry.

However, one may notice that the Doppler factor associated with a Raman feature is affected by the relative motion between the emitter and the hydrogen atom and is almost independent of the observer’s line of sight. If an emission region is aspherical, such as toroidal or bipolar with an inclination angle i with respect to the observer’s line of sight, direct emission spectroscopy yields somewhat lower velocity width involving

the factor $\sin i$. In contrast, atomic Raman spectroscopy reflects only the relative speed of H I and He II with no underestimation of the expansion speed due to the $\sin i$ factor.

IC 5117 exhibits a bipolar nebular morphology, and the H I region would be more appropriately approximated by a cylindrical shell than a spherical one (Hsia et al. 2014). More reasonable analyses can be performed with an adoption of a cylindrical shell model including the projection effects to the celestial sphere. We will investigate this model with consideration of polarization in the near future.

4. Summary and Discussion

We investigate line formation of Raman-scattered He II λ 4851 in an expanding spherical H I shell that may be found in young PNe and symbiotic stars. In this work, we take into careful consideration the change in cross section that occurs as the Doppler factor of a photon varies along the propagating path in a moving medium. In a spherically expanding medium, all of the hydrogen atoms move away from each other. Therefore, in the rest frame of any hydrogen atom, line photons get redshifted toward Ly γ resonance, at which the scattering cross section increases sharply. This leads to significant enhancement in the Raman conversion efficiency compared to the case of a static H I medium, as is illustrated in Figure 6. Another notable effect of expansion of the neutral region is frequency redistribution, which tends to strengthen the red part of the emergent Raman He II feature by systematically redshifting line photons.

It is found that the line profiles are mainly characterized by an asymmetric double-peak structure with a significant red tail that may extend to the line centers of He II λ 4859 and H β . The extended tail part is contributed by photons that have acquired a significant Doppler factor through one or a few Rayleigh reflections at the inner surface of the neutral shell. Blending with these two strong emission lines may severely hinder observational investigation of the extended red tail part. In particular, young PNe and symbiotic stars exhibit broad wings around Balmer emission lines, which also make it difficult to isolate a clear profile of Raman-scattered He II λ 4851 (Lee & Hyung 2000; Chang et al. 2018). Incomplete subtraction of Balmer wings may lead to an erroneous estimate of Raman conversion efficiency.

In this work, a new grid-based Monte Carlo code has been developed in order to take into account the H I density variation along a photon path. This code is quite flexible, so it will be adopted to investigate line formation of Raman-scattered O VI at 6825 Å and 7082 Å found in many symbiotic stars. In these objects, Raman scattering takes place in a slow stellar wind from the giant component suffering a heavy mass loss. Important kinematic information of the H I component will be revealed through detailed line profile analyses of Raman O VI features (e.g., Schmid 1996; Heo et al. 2016; Lee et al. 2019).

Due to the resonance nature in the scattering cross section and branching ratios varying with wavelength, we obtain very diverse line profiles and Raman conversion efficiencies. In this respect, it is very desirable to obtain high-quality spectroscopic data of objects exhibiting Raman-scattered He II features. With these high-quality data, we may expect to secure faint Raman He II features formed blueward of high Balmer series lines, including H γ and H δ . Much more detailed information will be gained if one can compare as many Raman-scattered He II features as possible using instruments with wide spectral

coverage. For example, the line centers of Raman He II are affected by both atomic physics and the kinematics of the H I region. One way to isolate one effect from the other is to compare line centers of two or more Raman He II features.

A significant fraction of planetary nebulae exhibit a bipolar nebular morphology (Sahai et al. 2011), for which the circumnebular neutral region is approximated by a cylindrical shell rather than a spherical shell. In the case of a neutral cylindrical shell, the emergent Raman-scattered He II features can be polarized depending on the H I column density and the orientation of the cylinder with respect to the observer's line of sight. In this case, the emergent profiles also depend on the observer's line of sight.

Considering that young PNe reported for detection of Raman-scattered He II are also molecular line emitters, it will be very interesting to carry out high-resolution spectroscopy of molecular lines. Taylor et al. (1990) suggested three possible mechanisms responsible for the formation of a neutral atomic region. One mechanism invokes atomic stellar winds that may occur in the AGB stage, while the others involve the dissociation of molecular stellar winds either by UV radiation from the hot central star or by the ambient interstellar UV radiation field. In particular, if the H I region is inside the molecular region, the kinematic properties of the neutral shell and of the molecular region are strongly correlated. Two-dimensional spectroscopy using an integrated field unit is expected to provide interesting observational data.

The authors are very grateful to the anonymous referee who provided constructive and helpful comments. This work is based on observations obtained at the Canada–France–Hawaii Telescope (CFHT), which is operated by National Research Council of Canada, the Institut National des Sciences de l'Univers of the Centre National de la Recherche Scientifique of France, and the University of Hawaii. This research was supported by the Korea Astronomy and Space Science Institute under the R&D program (Project No. 2018-1-860-00) supervised by the Ministry of Science, ICT and Future Planning. This work was also supported by a National Research Foundation of Korea (NRF) grant funded by the Korea government (MSIT; No. NRF-2018R1D1A1B07043944). This work was also supported by the K-GMT Science Program (PID: cfht_14BK002) funded through the Korea GMT Project operated by the Korea Astronomy and Space Science Institute.

ORCID iDs

Hee-Won Lee  <https://orcid.org/0000-0002-1951-7953>

References

- Akras, S., Guzman-Ramirez, L., Leal-Ferreira, M. L., & Ramos-Larios, G. 2019, *ApJS*, 240, 21
- Allen, D. A. 1980, *MNRAS*, 190, 75
- Bethe, H. A., & Salpeter, E. E. 1967, *Quantum Mechanics of One and Two Electron Atoms* (New York: Academic Press Inc.)
- Birriel, J. J. 2004, *ApJ*, 612, 1136
- Chang, S.-J., Lee, H.-W., Lee, H.-G., Ahn, S.-H., & Park, B.-G. 2018, *ApJ*, 866, 129
- Dinerstein, H. L. 1991, *PASP*, 103, 861
- Groves, B., Dopita, M., Williams, R., et al. 2002, *PASA*, 19, 425
- Gussie, G. T., & Taylor, A. R. 1995, *MNRAS*, 273, 801
- Heo, J.-E., Angeloni, R., Di Mille, F., Palma, T., & Lee, H.-W. 2016, *ApJ*, 833, 286
- Höfner, S., & Olofsson, H. 2018, *A&ARv*, 26, 1
- Hsia, C. H., Chau, W., Zhang, Y., & Kwok, S. 2014, *ApJ*, 787, 25

- Hummer, D. G., & Storey, P. J. 1987, *MNRAS*, **224**, 801
- Jung, Y.-C., & Lee, H.-W. 2004, *MNRAS*, **355**, 221
- Kang, E.-H., Lee, B.-C., & Lee, H.-W. 2009, *ApJ*, **695**, 542
- Karzas, W. J., & Latter, R. 1961, *ApJS*, **6**, 167
- Kastner, J. H., Weintraub, D. A., Gatley, I., et al. 1996, *ApJ*, **462**, 777
- Kenyon, S. 1986, *The Symbiotic Stars* (Cambridge: Cambridge Univ. Press)
- Kwok, S., Purton, C. R., & FitzGerald, P. M. 1978, *ApJ*, **219**, 125
- Lee, H.-W., & Hyung, S. 2000, *ApJL*, **530**, L49
- Lee, H.-W., Jung, Y.-C., Song, I.-O., et al. 2006, *ApJ*, **636**, 1045
- Lee, H.-W., Kang, Y.-W., & Byun, Y.-I. 2001, *ApJL*, **211**, L121
- Lee, Y.-M., Lee, H.-W., Lee, H.-G., & Angelono, R. 2019, *MNRAS*, **487**, 2166
- Nussbaumer, H., Schmid, H. M., & Vogel, M. 1989, *A&A*, **211**, L27
- Péquignot, D., Baluteau, J., Morisset, C., et al. 1997, *A&A*, **222**, 217
- Rodríguez, L. F., García-Barreto, J. A., Cantó, J., et al. 1985, *MNRAS*, **215**, 353
- Rodríguez, L. F., Goss, W. M., & Williams, R. 2002, *ApJ*, **574**, 179
- Sadeghpour, H. R., & Dalgarno, A. 1992, *JPhB*, **25**, 4801
- Sahai, R., Morris, M. R., & Villar, G. G. 2011, *AJ*, **141**, 134
- Sakurai, J. J. 1967, *Advanced Quantum Mechanics* (Reading, Massachusetts: Addison-Wesley Publishing Company)
- Schmid, H. M. 1989, *A&A*, **211**, 31
- Schmid, H. M. 1996, *MNRAS*, **282**, 511
- Smith, E. C. D., & McLean, I. S. 2008, *ApJ*, **676**, 408
- Stenflo, J. O. 1980, *A&A*, **84**, 68
- Storey, P. J., & Hummer, D. G. 1995, *MNRAS*, **272**, 41
- Taylor, A. R., Gussie, G. T., & Goss, W. M. 1989, *ApJ*, **340**, 932
- Taylor, A. R., Gussie, G. T., & Pottasch, S. R. 1990, *ApJ*, **351**, 515
- Treffers, R. R., Fink, U., Larson, H. P., & Gautier, T. N., III 1976, *ApJ*, **209**, 793
- van Groningen, E. 1993, *MNRAS*, **264**, 975
- Weinberger, R. 1989, *A&AS*, **78**, 301